Atmos. Meas. Tech., 17, 6807–6817, 2024
https://doi.org/10.5194/amt-17-6807-2024
© Author(s) 2024. This work is distributed under
the Creative Commons Attribution 4.0 License.

Atmospheric Measurement Techniques
Open Access

Consideration of the cloud motion for aircraft-based stereographically derived cloud geometry and cloud top heights

Lea Volkmer[1], **Tobias Kölling**[1,a], **Tobias Zinner**[1], **and Bernhard Mayer**[1]

[1]Meteorologisches Institut, Ludwig-Maximilians-Universität München, Munich, Germany
[a]now at: Climate Physics, Max Planck Institute for Meteorology, Hamburg, Germany

Correspondence: Lea Volkmer (l.volkmer@physik.uni-muenchen.de)

Received: 9 February 2024 – Discussion started: 26 February 2024
Revised: 9 October 2024 – Accepted: 14 October 2024 – Published: 4 December 2024

Abstract. Cloud geometry and in particular cloud top heights can be derived from 2-D camera measurements by applying a stereographic method to data from an overflight over a scene of clouds (see, e.g., Kölling et al., 2019). Although airplane overpasses are relatively fast, cloud motion with the wind is important and can result in errors in the cloud localization. Here, the impact of the wind is investigated using the method from Kölling et al. (2019) for measurements of the airborne hyperspectral imaging system spectrometer of the Munich Aerosol Cloud Scanner (specMACS). Further, a method for cloud motion correction using model winds from the European Centre for Medium-Range Weather Forecasts (ECMWF) is presented. It is shown that the update is important as the original algorithm without the cloud motion correction can over- or underestimate the cloud top heights by several hundred meters, depending on the wind speed and the relative wind direction. This is validated using data from the Elucidating the role of clouds–circulation coupling in climate (EUREC^{4}A) campaign and realistic 3-D radiative transfer simulations. From the comparison of the derived cloud top heights with the expected ones from the model input, an average accuracy of the cloud top heights of less than (20 ± 140) m (mean deviation and 1 standard deviation) is estimated for the updated method.

1 Introduction

The macro- and microphysical properties of clouds have a large impact on the Earth's radiation and energy budgets as they determine the clouds' interaction with solar and terrestrial radiation. Since clouds have a high spatial and temporal variability, representing them accurately in both numerical weather prediction and global climate models is difficult such that parameterizations of the cloud properties are important. These parameterizations often rely on observational studies that have been widely extended in recent decades. In particular, one aim has been to obtain a better understanding of the role of clouds in climate change. An important contribution to the characterization of cloud properties is provided by active and passive remote sensing instruments, which can be ground-, aircraft- or satellite-based and sensitive to different wavelengths in both the solar and the terrestrial spectral range. One of these instruments is the airborne spectrometer of the Munich Aerosol Cloud Scanner (specMACS; Ewald et al., 2016; Pörtge et al., 2023; Weber et al., 2024) operated on board the German High Altitude and LOng range research aircraft HALO (Krautstrunk and Giez, 2012). specMACS consists of two hyperspectral line cameras measuring radiances in the wavelength range between 400 and 2500 nm (Ewald et al., 2016) and two polarization-resolving RGB cameras (Phoenix 5.0 MP Polarization Model) (Pörtge et al., 2023; Weber et al., 2024). In this manner, the solar radiation reflected from clouds is measured with a high spectral and spatial resolution and a wide field of view (32.7 and 35.5° for the line cameras, Ewald et al., 2016, and $91° \times 117°$ for the two polarization cameras combined, Weber et al., 2024). The specMACS measurements are used for microphysical retrievals of cloud properties, using both a bispectral approach as described by Nakajima and King (1990) and a polarimetric retrieval described by Pörtge et al. (2023), which uses multi-angle polarized radiance observations of the cloudbow to derive cloud droplet size distributions (CDSDs). In general, passive observations usually do not provide cloud top height

or structure with height resolution. However, for the interpretation and geolocalization of the microphysical retrievals, the exact location of the observed clouds in 3-D space is important. To this end, stereographically derived cloud geometry is used.

One approach for the localization of clouds in 3-D space is stereographic reconstruction from multi-angle intensity measurements while flying over a scene of clouds. For example, this has been used for spaceborne instruments such as the Multi-angle Imaging SpectroRadiometer (MISR) (Moroney et al., 2002; Seiz and Davies, 2006) and the Advanced Spaceborne Thermal Emission and Reflection Radiometer (ASTER) (Seiz et al., 2006). For specMACS, the clouds are located in 3-D space using the 2-D intensity measurements of the polarization cameras. The algorithm is described in detail by Kölling et al. (2019) and is based on the identification of points on the cloud surface using contrast gradients. Afterward, the points are re-identified in subsequent images and located in 3-D space using the multi-angle observation. Then, the derived cloud top heights are for example used for the geolocalization of the cloud targets observed by the polarimetric retrieval for the determination of the CDSD. The retrieval is based on the aggregation of the polarized radiance measured for a cloud target in subsequent images to obtain the full signal of the cloudbow, which is sensitive to both the effective radius and the variance of the CDSD. Thereby, accurate cloud top heights are important as small errors in the cloud top height assigned to cloud targets will lead to wrong localizations of the targets in subsequent images. Consequently, this leads to a wrong aggregation of the cloudbow signal and thus errors in the derived CDSD (Pörtge et al., 2023).

So far, stereographically retrieved cloud top heights have been compared by Kölling et al. (2019) to the cloud top heights derived from the WAter vapor Lidar Experiment in Space (WALES; Wirth et al., 2009) lidar for simultaneous measurements during the North Atlantic Waveguide and Downstream Impact Experiment (NAWDEX) campaign in October 2016. They found a median bias of 126 m, with the stereo heights found to be lower. It was indicated that the most prominent outliers in regions of high lidar cloud top height and low stereo height were observed for thin cirrus layers above cumulus clouds. In those scenes, the lidar is sensitive to the upper ice cloud layer, while the stereo algorithm detects image areas with high contrasts, which are preferably observed for lower cloud layers. Volkmer et al. (2024) applied the stereographic reconstruction algorithm to synthetic measurements obtained from realistic 3-D radiative transfer simulations and found an average underestimation of the stereographic cloud top heights by (70 ± 130) m without correcting for any cloud motion. Kölling et al. (2019) argued that, in contrast to the spaceborne methods employed, e.g., MISR (Moroney et al., 2002; Seiz and Davies, 2006) and ASTER (Seiz et al., 2006), no correction of the cloud wind movement needs to be applied. This is due to the much smaller time difference between two successive images (frame rate of 1 Hz used for the stereo algorithm) and the much lower operating altitude, leading to a much more rapid change in the observation angle compared to the satellite observations. However, the observation of the clouds from multiple viewing perspectives has been exploited to derive an estimate of the underlying 3-D wind field.

In subsequent evaluations of measurement data, the impact of the cloud motion on the stereographically derived cloud top heights was further investigated by comparing the derived cloud top heights for flight legs which were flown forward and backward within a time difference of about 70 min. Deviations of several hundred meters despite the temporally highly resolved observation of the clouds from multiple viewing angles have been observed. This is due to the faster movement of the clouds through the field of view of the instrument when the aircraft is flying against the wind and leads to an overestimation of the cloud top heights. Correspondingly, flying with the wind direction leads to an underestimation of the cloud top heights. Hence, an approach for the cloud motion correction using the 3-D wind field of the fifth-generation European Centre for Medium-Range Weather Forecasts (ECMWF) atmospheric reanalysis (ERA5; Hersbach et al., 2020) has been developed and is presented in Sect. 2 in this study. In Sect. 3, the cloud motion correction is validated using measurement data. Finally, the approach is validated using realistic 3-D radiative transfer simulations of the measurements performed with MYSTIC (Monte Carlo code for the physically correct tracing of photons in cloudy atmospheres; Mayer, 2009; Volkmer et al., 2024) in Sect. 4.

2 Wind correction based on ERA5 reanalysis data

To correct for the movement of clouds within the observation time, the ERA5 reanalysis data on 37 pressure levels between 1000 and 1 hPa on a regular latitude–longitude grid of $0.25° \times 0.25°$ are used. The data have a temporal resolution of 1 h (Hersbach et al., 2020). Only the horizontal wind movement is considered since the convective movement of the clouds observed by specMACS is not resolved in the ERA5 data.

The aircraft-based stereographic reconstruction of the 3-D cloud geometry is based on the observation of clouds from different perspectives by flying over them. Points on the cloud surface are identified using contrasts and then re-identified in subsequent images using the optical flow algorithm described by Lucas and Kanade (1981). Then, the points are located in 3-D space using a triangular geometry as schematically shown in Fig. 1. In order to correct for cloud motion, the wind vector $\boldsymbol{v}$ at the cloud location is needed, which, however, is not known yet. Hence, the stereographic reconstruction is performed iteratively by first calculating the location of the point without considering the movement

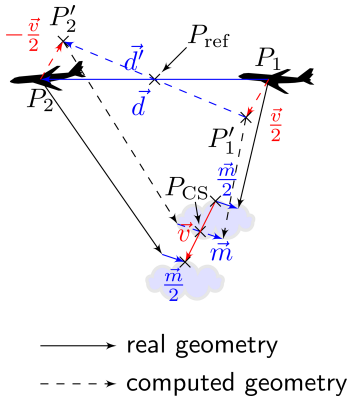

Figure 1. Tracking geometry for the location of the points on the cloud surface as in Kölling et al. (2019) but with the modification for the cloud motion correction. The real geometry is shown by the solid vectors, while the actually computed geometry is visualized by the dashed vectors. Hereby, $\boldsymbol{v}$ denotes the wind vector at P_{CS}. The vector $\boldsymbol{d}$ refers to the distance vector between the two aircraft positions (typically around 200 m), and $\boldsymbol{d}'$ is the corresponding quantity for the modified geometry. The point P_{ref} is the reference viewing point from which the point on the cloud P_{CS} is observed. Finally, $\boldsymbol{m}$ is the so-called mispointing vector, which takes into account that two straight lines in 3-D space do not necessarily meet. However, its length is only of the order of a few meters.

of the observed cloud as described in Kölling et al. (2019). Next, the horizontal wind vector is estimated at the location where the point was found at the cloud surface and the corresponding time of observation by linear interpolation of the gridded reanalysis data.

Afterward, the calculation of the point is repeated with the estimated cloud motion. To do so, the aircraft's locations are virtually shifted with half of the wind vector, which ensures that the point identified on the cloud surface is located in between the two actual locations as it is still observed under the same viewing angles. This is schematically depicted in Fig. 1. The two real aircraft positions at $P_1 = (t, \boldsymbol{x})$ and $P_2 = (t + \Delta t, \boldsymbol{x} + \Delta \boldsymbol{x})$ from which the cloud is observed are moved with the horizontal wind vector obtained from the interpolation of the ERA5 data at the initially estimated cloud top height. The initial viewing points P_1 and P_2 are shifted to the points $P_1' = \left(t, \boldsymbol{x} + \frac{\Delta t}{2}\boldsymbol{v}\right)$ and $P_2' = \left(t + \Delta t, \boldsymbol{x} + \Delta \boldsymbol{x} - \frac{\Delta t}{2}\boldsymbol{v}\right)$. Using this modification guarantees that the reference point P_{ref} for the observer location remains the same. With this modified geometry, the location of the point on the cloud surface (P_{CS}) is calculated again. Since the wind vector can only be estimated at the cloud surface height location initially found by the method, the correction is iterated five times. Hereby, a stepwise-corrected height for the estimation of an improved wind vector is used each time. It has been found that more iteration steps do not improve the result significantly.

An additional uncertainty in the stereographically estimated cloud top height is the accuracy of the ERA5 wind data, which has been studied by comparisons to observations: for the surface wind field, Belmonte Rivas and Stoffelen (2019) found systematic differences of up to 0.5 m s^{-1} in the mean zonal and meridional components compared to the ocean vector winds of the Advanced Scatterometer (ASCAT). Hereby, the mean zonal winds are found to be overestimated, whereas the mean meridional winds are found to be underestimated. Savazzi et al. (2022) and Wu et al. (2024) performed regional comparisons of the ERA5 wind. Savazzi et al. (2022) used dropsonde, radiosonde and wind lidar measurements from the Elucidating the role of clouds–circulation coupling in climate (EUREC^{4}A) campaign to evaluate the wind bias in the lower troposphere in January and February 2020. They found root mean square errors (RMSEs) up to 2 m s^{-1} and a mean wind speed bias up to -0.5 m s^{-1} in the lower 5 km of the atmosphere. Similar results with mean wind vector differences of 2.0–3.0 m s^{-1} were found by Wu et al. (2024) in comparisons of the ERA5 winds to dropsondes from the Convective Processes Experiment – Aerosols and Winds (CPEX-AW) campaign and radiosondes of the Southern Great Plains (SGP) atmospheric observatory between 400 and 850 hPa.

The maximum error in cloud top height due to wind uncertainty Δh can be estimated using the following formula:

$$\Delta h = \frac{h_{\mathrm{a}} - h_{\mathrm{c}}}{\frac{v_{\mathrm{a}}}{\Delta v} - 1}. \tag{1}$$

Here, h_{a} denotes the height of the aircraft, h_{c} is the cloud top height, v_{a} is the speed of the aircraft and Δv is the error in the wind speed aligned with the aircraft's flight direction. For the maximal difference of 3 m s^{-1} found in the mentioned studies, this would result in an additional cloud top height uncertainty of about 150 m if we assume an aircraft–cloud distance of 10 km and an aircraft speed of 200 m s^{-1}, which are typical for the HALO aircraft. We show later in the paper that such a large value is not found in comparisons using data from the EUREC^{4}A campaign but rather values equivalent to a wind speed bias of 0.5 m s^{-1}.

3 Validation using measurements from the EUREC^{4}A campaign

The validation of the cloud motion correction on the cloud top heights derived by the stereographic reconstruction algorithm described above was conducted by considering two consecutive straight flight legs flown by HALO toward the Northwest Tropical Atlantic Station (NTAS) buoy, located at about 15° N and 51° W (Stevens et al., 2021), and back on 28 January 2020 during the EUREC^{4}A campaign. As described by Stevens et al. (2021), that day was associated with shallow cumulus clouds, which could also be observed on the two mentioned straight legs. There were no additional cloud

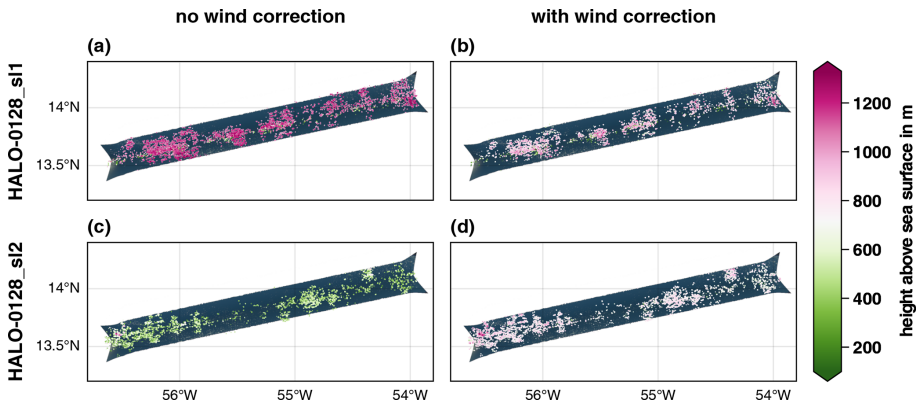

Figure 2. Example of the cloud motion correction of the stereographically retrieved cloud top heights of the flight segments HALO-0128_sl1 and HALO-0128_sl2 during the EUREC^{4}A campaign. The legs were flown to the NTAS buoy on 28 January 2020 and directed toward the northeast such that the leg toward the buoy (sl1) was flown approximately against the wind while the wind was moving the clouds in the flight direction on the way back. On the left, the stereographically retrieved cloud top heights without cloud motion correction are shown for both legs. On the right, the cloud motion correction based on the ERA5 reanalysis data is included. The background shows images from the two polarization-resolving cameras of specMACS projected onto a surface at 1 km altitude.

layers above the low shallow cumuli, and hence the signal measured by specMACS and the backscatter signal measured by the WALES lidar operated simultaneously on HALO originate from the same cloud targets. Thus, the derived cloud top heights should show good agreement. The straight legs were chosen for the validation because the NTAS buoy was located in the northeast of the standard EUREC^{4}A circle flown by HALO (Stevens et al., 2021). Given the prevailing north-easterly trade winds in this region at that time of the year, the first leg toward the buoy (HALO-0128_sl1) is flown against the wind, while immediately afterward the return leg (HALO-0128_sl2) is flown with the wind. The two legs were each about 20 min long, corresponding to a flight distance of about 270 km. The time difference between the start of the first leg and the end of the second leg (the maximum time difference for a given position in the following analysis) was about 70 min. WALES measurements, which are not affected by the cloud movement, showed no significant changes in cloud top height during this time, with median values of about 745 m on the first leg and 738 m on the second one.

Figure 2 shows the retrieved cloud top heights from the two consecutively flown straight legs projected onto specMACS images of the respective flight legs. The corresponding histograms are given in Fig. 3, including the histograms and the median of the cloud top heights derived from measurements of the WALES lidar using all measurements which are referred to as most likely cloudy (Wirth, 2021). It can be seen that the stereographically derived cloud top heights on the way to the NTAS buoy and back differ by more than 600 m in the median without any cloud motion correction. This is due to the overestimation of the cloud top heights on the way to the buoy while flying against the wind and the underestimation on the downwind-directed way back. The total horizontal wind speed was about 7 m s^{-1}, as measured by a dropsonde launched from HALO at the end of the first leg. Including the cloud motion correction based on the ERA5 reanalysis data results in a shift of the stereographically derived cloud top heights to lower (HALO-0128_sl1) and higher (HALO-0128_sl2) values such that the median values only differ by less than 60 m. Thus, they are now of the same order of magnitude considering that clouds that are not exactly the same are observed on both legs and that they might develop over time. Finally, a comparison to the histograms and the median values of the lidar heights shows much better agreement for the wind-corrected heights. The difference between the stereographically derived cloud top heights and the median of the WALES measurements reduces from about ±300 m without the cloud motion correction to about 50 m on the way to the buoy and about 3 m on the way back when the cloud motion correction is included.

4 Accuracy estimation using realistic simulated measurements from 3-D radiative transfer simulations

To further constrain the accuracy of the presented method, realistic 3-D radiative transfer simulations with the radiative transfer model MYSTIC (Mayer, 2009; Emde et al., 2010) as part of the libRadtran radiative transfer package (Mayer and Kylling, 2005; Emde et al., 2016) were performed, and the stereographic reconstruction algorithm was applied to the simulated measurements of a 1 min overflight over a field of large-eddy-simulated (LES) shallow cumulus clouds as presented by Volkmer et al. (2024). The radiative transfer simulations were conducted for the LES cloud field with a horizontal extent of $25.6 \times 12.8\,\mathrm{km}^2$ at a horizontal resolution

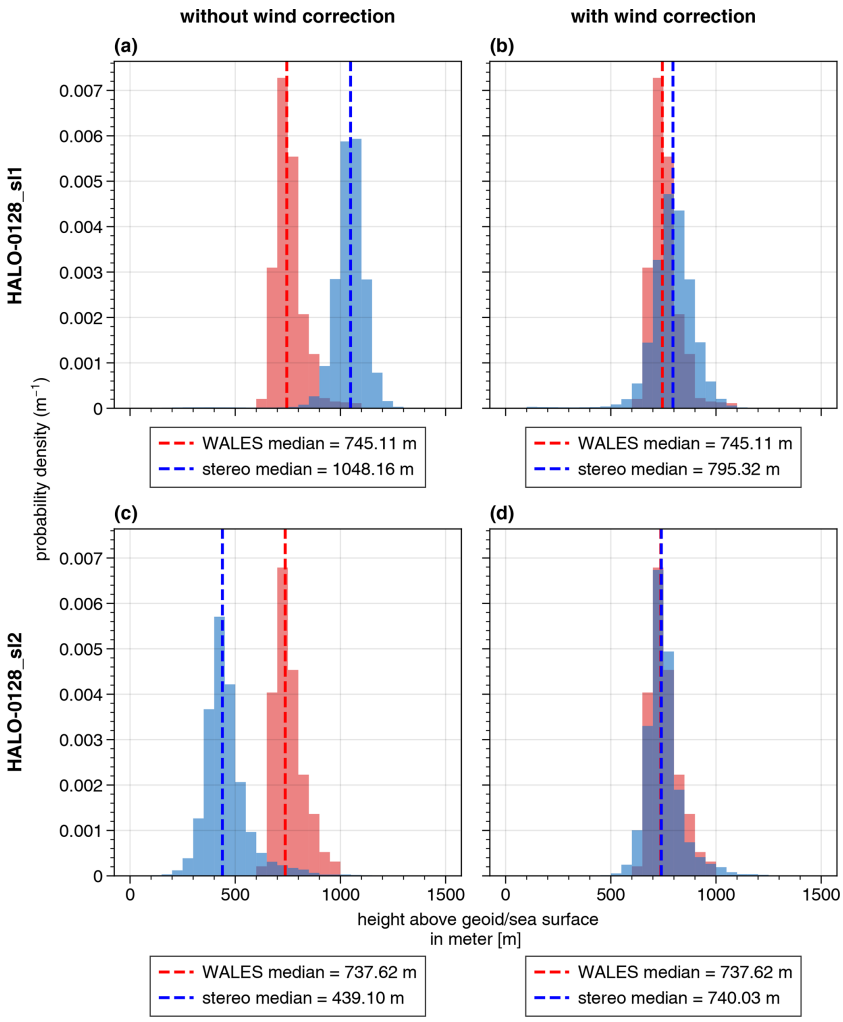

Figure 3. Histograms of the stereographically retrieved cloud top heights (blue) and the corresponding histograms of the WALES lidar cloud top height measurements (red) of the flight segments HALO-0128_sl1 and HALO-0128_sl2 as described in Fig. 2. On the left **(a, c)**, the histograms of the stereographically retrieved cloud top heights without cloud motion correction are shown for both legs. On the right **(b, d)**, the cloud motion correction based on the ERA5 reanalysis data is included. Next to the median of the stereographically derived cloud top heights (dashed vertical blue line), the median of the cloud top heights derived by the WALES lidar is shown (red line).

of 20 m and a vertical resolution of about 25 m. A flight altitude of 10 km was assumed. Figure 4 shows the underlying model wind field as obtained from the large-eddy simulations, indicating wind directions between approximately 140° at low altitudes and 340° at higher altitudes. The average wind speed is between 0.6 m s^{-1} at about 2500 m and 3.2 m s^{-1} between 100 and 900 m and hence smaller overall than for the real measurements considered before. The aircraft was simulated to fly toward the north with a horizontal aircraft alignment (all three Euler angles are zero). This corresponds to a mainly downwind flight direction for clouds lower than about 2400 m where the wind direction exceeds 270°.

For the comparison of the model heights to the stereographically derived cloud top heights, we used the same method as presented by Volkmer et al. (2024). The expected cloud top heights were obtained from the first scattering events of Monte Carlo-based reference simulations, where the photons are started at the detector. For each simulated pixel, 1000 photons were computed, and the scattering events of all photons not scattered at the ground were averaged to determine the height from where the optical signal originates. In Fig. 5 the expected model heights (Fig. 5a) and the corresponding stereographically derived cloud top heights including the cloud motion correction (Fig. 5c) are shown for the simulated measurements together with their respective histograms (Fig. 5b and d). On the left, the points found are projected onto the measurement simulated after a flight time of 30 s. The flight direction is to the right of the simulated measurement. Mean cloud top heights of about 1628 m for

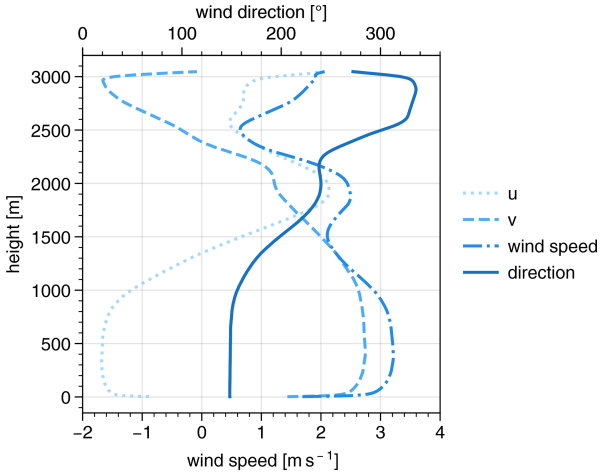

Figure 4. Average vertical profiles of the horizontal wind vector of the LES cloud field after a simulation time of 30 s. The horizontal wind speed and the u and v components are shown with respect to the lower axis, while the wind direction is shown with regard to the upper axis.

the expected model heights and 1644 m for the stereographically derived cloud top heights are found. On the bottom of Fig. 5, the pointwise difference between the stereographic heights and the model heights is shown (Fig. 5e). From all pointwise differences, a mean difference of about 15 m between the stereo and model heights and a standard deviation of about 133 m is derived as shown in the corresponding histogram in Fig. 5f. Without any cloud motion correction, the stereographically derived cloud top heights for the considered LES cloud field deviated on average by (-70 ± 130) m from the expected cloud top heights of the model input (Volkmer et al., 2024). Thus, the effect of the wind consideration is approximately 85 m for the given cloud field and aircraft direction, with a wind speed of about 2 m s^{-1} in the flight direction. This is in accordance with the expectation from Eq. (1), resulting in a theoretical underestimation of the cloud top heights of about 84.4 m s^{-1}, when inserting the prescribed aircraft height of 10 000 m, the mean cloud top height of about 1600 m and the simulated aircraft speed of 200 m s^{-1}. It can again be observed that the pointwise differences between the stereographically derived cloud top heights and the model heights can be up to ± 500 m, with the positive values occurring more frequently where the cloud is generally lower (at the cloud edges and in shadowed regions), while the negative ones are observed at the highest cloud tops.

5 Discussion

In our analysis, we could reduce the absolute mean bias in the stereographic cloud top height retrieval applied to simulated measurements from radiative transfer simulations to approximately 15 m, when including the wind movement of the clouds. However, the standard deviation, which shows the spread of the single measurements, remains at about 130 m with and without wind correction. One possible error source, the evolution of the observed clouds, has been studied by Volkmer et al. (2024) using a similar setup as described above but with non-developing and non-moving clouds. Hereby, an absolute mean bias of (46 ± 140) m was found. While the larger mean bias might be explained by a remaining uncertainty in the wind estimation and a cancellation of the error sources, the standard deviation, and hence the error of the single measurement, remains approximately constant. One explanation for this could be the method of comparison between the stereographically determined cloud top heights and the model heights. The model heights were derived from single-scattering reference simulations, and hence the simulated photons are on average scattered at an optical depth of about unity (Volkmer et al., 2024). This is valuable because optical phenomena such as the cloudbow arise from single scattering (Alexandrov et al., 2012), and thus, for an accurate application of the polarimetric retrieval (Pörtge et al., 2023), the cloud top heights derived by the stereographic retrieval should correspond best to the heights where the polarized cloudbow signal originates from. Moreover, in Volkmer et al. (2024) it is argued that the stereo algorithm detects contrasts which will not be visible deeper into the cloud and that the signal smooths out when multiple scattering becomes more important. To further address this issue, we can use the model simulations to calculate the actual optical thickness at which the stereo points are found. To do so, we used the camera configuration after 30 s of simulation time, which is also used for the comparison between the stereo and the model heights. From Fig. 6 it can be seen that the optical thickness along the viewing directions of the given simulation time where the stereo points are found varies between about 0 and 25 with a median of 0.71 and a mean of 3.07. Further, Fig. 6c indicates that the stereo points are mostly estimated too high where the optical thickness is small (i.e., below 1) and that they are estimated too low for larger optical thicknesses. This is in accordance with the observation that the stereo points are usually estimated too low in the center of the clouds where they are found at larger optical thicknesses and too high at the cloud edges where the optical thicknesses are small (Figs. 5e and 6a).

Real measurements include further uncertainties due to limitations in the geometric camera calibration (Kölling et al., 2019, Appendix A): at a cloud–aircraft distance of 10 km, a relative change of 0.01° (1/3 px for the old 2-D RGB camera and about 1/4 px for the new polarization cameras; Weber et al., 2024) in the viewing angle results in a wrongly calculated distance between the aircraft and the cloud of 100 m. As described by Weber et al. (2024), the current geometric calibration of the polarization cameras of specMACS shows mean root mean square reprojection errors of the best-fitting camera model of 0.18 px for the polLL camera and 0.20 px for the polLR camera. Hence, this results

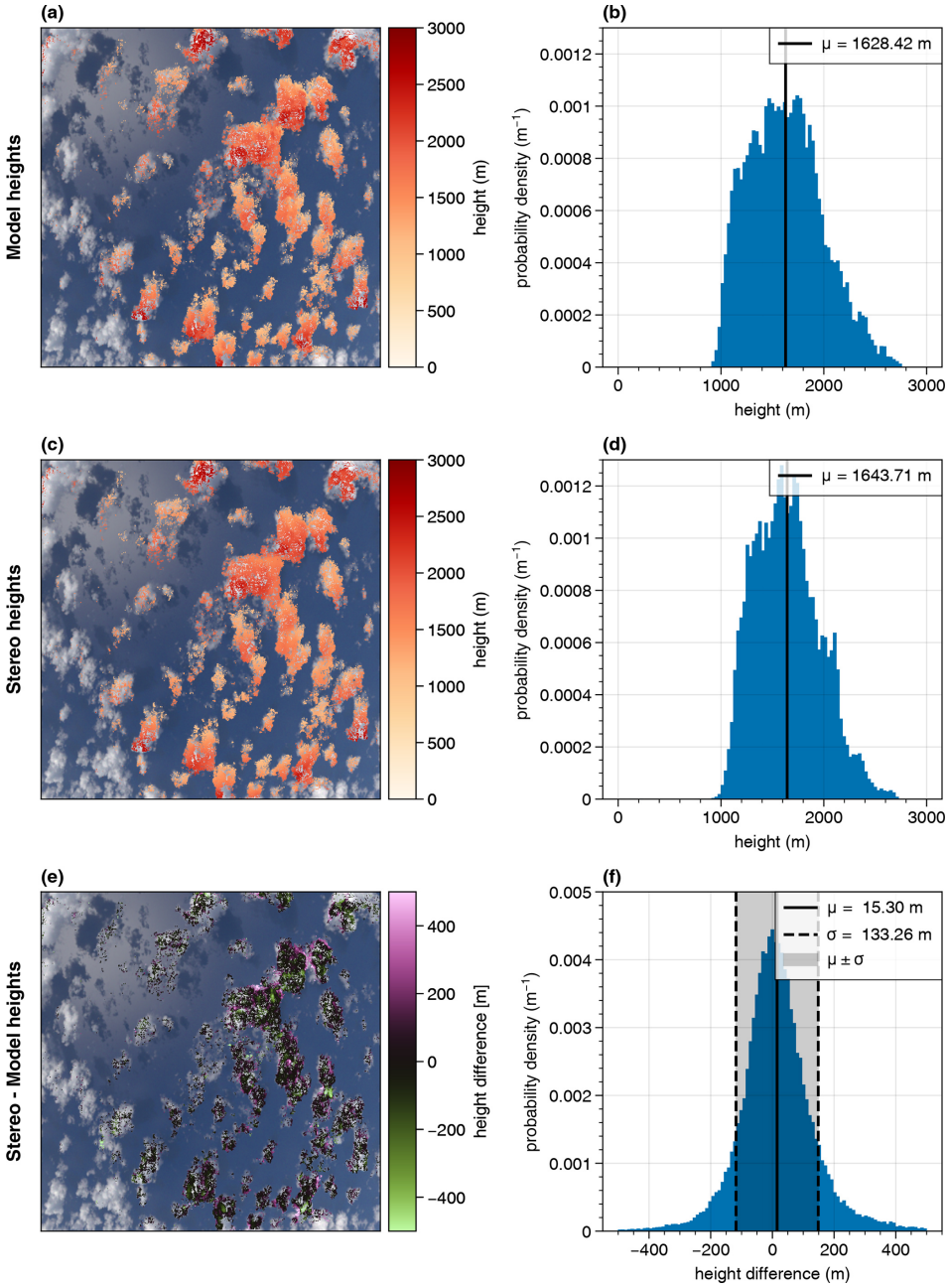

Figure 5. Comparison of the cloud top heights expected from the model and derived from the stereographic reconstruction algorithm. The cloud top heights as expected from the model input (model heights) are shown in panel **(a)** (only for points where the stereo method provided information). The stereographically derived cloud top heights can be seen in panel **(c)**. Below, the pointwise differences are shown **(e)**. The derived points were projected onto the simulated RGB image, and the corresponding histograms are shown in panels **(b)**, **(d)** and **(f)**. The solid vertical lines indicate the mean values. The dashed vertical lines in panel **(f)** refer to the boundaries of the $\mu \pm \sigma$ interval.

in an additional error of about 70 m due to the geometric calibration, which is not taken into account in this (model) study.

Stereographic cloud top height retrievals are also applied to MISR (Moroney et al., 2002; Seiz and Davies, 2006) and ASTER (Seiz and Davies, 2006) measurements. Mitra et al. (2021) performed a detailed error analysis of the MISR cloud top heights by comparing them to lidar measurements. The total error for MISR cloud top heights is estimated to be (-280 ± 370) m for optically thick, single-layered and unbroken clouds, and the precision is driven by the accuracy of the derived MISR wind speed of $3.7\,\mathrm{m\,s^{-1}}$ (Mitra et al., 2021). For ASTER, Seiz et al. (2006) found a systematic error of 12.5 m with an additional uncertainty of about 100 m for every $1\,\mathrm{m\,s^{-1}}$ uncertainty in the wind component along the

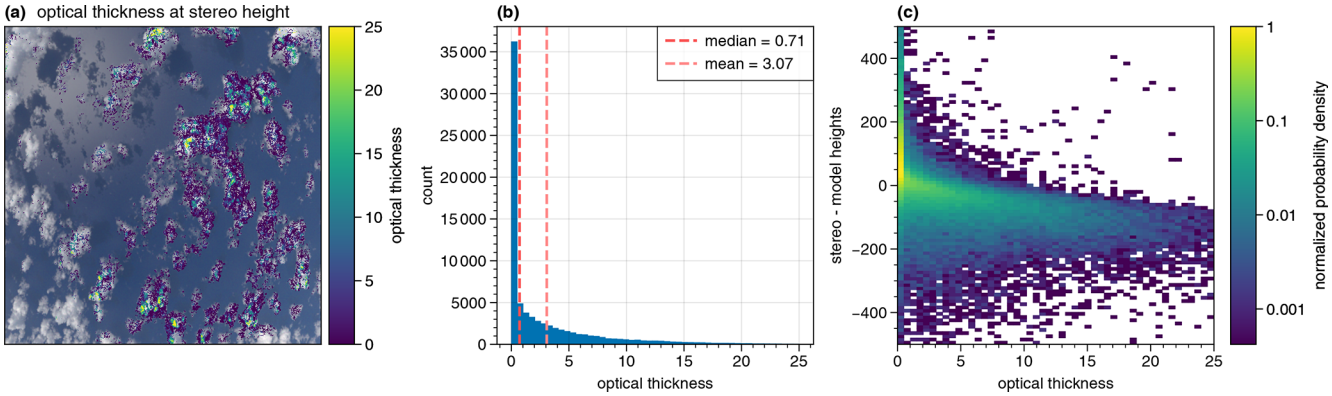

Figure 6. Optical thickness derived from the model input at which the stereographically derived points are found for the viewing geometry after a simulation time of 30 s. In panel **(a)**, the optical thickness found for the stereo points is projected onto the corresponding simulated RGB image. In panel **(b)**, the corresponding histogram of the optical thickness is shown. Panel **(c)** shows the 2-D histogram of the difference between the stereo and the model heights with regard to the optical thickness at which the stereo points are found. Note that the color scale in **(c)** is logarithmic.

track of the satellite. In the future, using the wind speed derived from the stereographic retrieval of specMACS (Kölling et al., 2019) for the correction of the cloud movement might also be possible. Hereby, the performed model simulations would allow us to test the accuracy of the stereo wind and further to investigate how its usage as a cloud movement correction affects the stereo cloud top height accuracy. Depending on the performance of the derived cloud movement, this would also affect the accuracy of the stereographically derived cloud top heights. As stated above, the deviation of the ERA5 wind speed from observations is of the order of 2–3 $\mathrm{m\,s^{-1}}$, and a convective development of the clouds is not taken into account. Hence, the determined stereographic cloud top height might be improved by using the stereographically derived wind vector directly.

Furthermore, Mitra et al. (2021) investigated the error in the cloud top heights with regard to the cloud height, the presence of multi-layered clouds and the optical thickness of the observed clouds. One general problem of the stereographic method is that thin clouds and clouds or cloud parts with a lack of contrast (e.g., homogenous cirrus clouds) are not recognized by the algorithm. Hence, in these situations only lower cloud layers will be recognized if present, and compared to, e.g., lidar measurements, the cloud top heights will be estimated too low (Kölling et al., 2019). For MISR, Mitra et al. (2021) found that the lower layer is detected when the optical depth of the upper layer is smaller than about 0.3. Investigations into the extent to which multi-layered clouds are recognized by the specMACS stereographic algorithm are also planned for the future. Moreover, clouds over ice, i.e., over sea ice in the Arctic or snow-covered land, are not seen by the stereographic method because of the lack of contrast between the surface and the cloud, which was frequently observed during the HALO-(AC)^3 campaign (Wendisch et al., 2024). Here, an analysis of the detection of clouds over snow or ice using the specMACS measurements would be valuable.

6 Conclusions

In this paper, we presented an improvement of the stereographic reconstruction method for the determination of 3-D cloud geometry using measurements of specMACS as developed by Kölling et al. (2019). The improvement of the method includes the estimation of the cloud wind movement using ERA5 reanalysis data. It could be shown that the consideration of the cloud movement with the wind is important for the estimated cloud top heights. Without any cloud motion correction, the cloud top heights from two flight legs deviated by more than 600 m depending on the wind direction, while the median of the cloud top heights derived from measurements of the WALES lidar remained approximately constant. With the consideration of the cloud motion, much better agreement between the stereographically derived cloud top heights and the ones from the WALES measurements could be achieved, with median differences of about 50 m for the first leg and less than 3 m on the way back.

The improvement in the derived cloud top heights when the wind movement is considered could also be validated using realistic 3-D radiative transfer simulations following the method from Volkmer et al. (2024). While the mean difference between the stereographically derived cloud top heights and the expected ones from the model input was (-70 ± 130) m without the consideration of the wind movement (Volkmer et al., 2024), the consideration of the cloud wind movement reduced the average difference to about (15 ± 133) m. Thus, while the mean bias is reduced, the spread, which can be taken as a measure for the single points, is approximately constant. The method used compares the stereographically derived cloud top heights to the

cloud top height at an optical thickness of approximately unity, which is the height where polarization features such as the cloudbow originate from. Hence, the accuracy of the cloud top heights from the 3-D stereographic reconstruction method, which are used for the derivation of cloud microphysical properties from the polarization measurements of specMACS (Pörtge et al., 2023), can be estimated to be better than (20 ± 140) m.

While this study is based on observed and simulated shallow cumulus clouds, the performance of the stereographic retrieval including the wind correction should in future also be tested for other cloud types. In particular, the retrieval should also work in more inhomogeneous cloud fields, with cloud tops spanning larger altitude ranges. This will be investigated in the future, using observations from past and upcoming field campaigns addressing different cloud types and corresponding simulated observations.

Data availability. The 3-D cloud geometry data from the stereographic reconstruction are available on the EUREC^{4}A database on the AERIS data server (https://doi.org/10.25326/508, Volkmer et al., 2023). The WALES (https://doi.org/10.25326/216, Wirth, 2021) and dropsonde data (https://doi.org/10.25326/246, George, 2021) are available on the database as well.

Author contributions. LV and TK implemented the wind correction in the stereographic reconstruction algorithm. LV applied the method to the measurements of the EUREC^{4}A campaign and processed and published the data. TK, TZ and BM actively participated in the EUREC^{4}A campaign and contributed to the paper. TZ and BM further helped develop the implementation of the wind correction by discussing the intermediate results.

Competing interests. At least one of the (co-)authors is a member of the editorial board of *Atmospheric Measurement Techniques*. The peer-review process was guided by an independent editor, and the authors also have no other competing interests to declare.

Disclaimer. Publisher's note: Copernicus Publications remains neutral with regard to jurisdictional claims made in the text, published maps, institutional affiliations, or any other geographical representation in this paper. While Copernicus Publications makes every effort to include appropriate place names, the final responsibility lies with the authors.

Acknowledgements. The authors thank the EUREC^{4}A campaign team for the organization, collaboration and support and the DLR flight operations team in particular for planning and executing the HALO flights. Moreover, we thank Andreas Giez, Vladyslav Nenakhov, Martin Zöger and Christian Mallaun for providing the high-temporal-resolution BAHAMAS data necessary for the accurate location of the points on cloud surfaces in 3-D space and the evaluation of the whole flights during the campaign. Furthermore, we thank Veronika Pörtge and Anna Weber for their contributions in the discussions and in particular for performing the measurements and evaluating the geometric calibration of the cameras. The data used in this publication were gathered during the EUREC^{4}A field campaign and are made available via the Meteorologisches Institut, Ludwig-Maximilians-Universität München.

Financial support. This research has been supported by the Deutsche Forschungsgemeinschaft (grant no. SPP 1294).

Review statement. This paper was edited by Ad Stoffelen and reviewed by Arka Mitra and three anonymous referees.

References

Alexandrov, M. D., Cairns, B., Emde, C., Ackerman, A. S., and van Diedenhoven, B.: Accuracy assessments of cloud droplet size retrievals from polarized reflectance measurements by the research scanning polarimeter, Remote Sens. Environ., 125, 92–111, https://doi.org/10.1016/j.rse.2012.07.012, 2012.

Belmonte Rivas, M. and Stoffelen, A.: Characterizing ERA-Interim and ERA5 surface wind biases using ASCAT, Ocean Sci., 15, 831–852, https://doi.org/10.5194/os-15-831-2019, 2019.

Emde, C., Buras, R., Mayer, B., and Blumthaler, M.: The impact of aerosols on polarized sky radiance: model development, validation, and applications, Atmos. Chem. Phys., 10, 383–396, https://doi.org/10.5194/acp-10-383-2010, 2010.

Emde, C., Buras-Schnell, R., Kylling, A., Mayer, B., Gasteiger, J., Hamann, U., Kylling, J., Richter, B., Pause, C., Dowling, T., and Bugliaro, L.: The libRadtran software package for radiative transfer calculations (version 2.0.1), Geosci. Model Dev., 9, 1647–1672, https://doi.org/10.5194/gmd-9-1647-2016, 2016.

Ewald, F., Kölling, T., Baumgartner, A., Zinner, T., and Mayer, B.: Design and characterization of specMACS, a multipurpose hyperspectral cloud and sky imager, Atmos. Meas. Tech., 9, 2015–2042, https://doi.org/10.5194/amt-9-2015-2016, 2016.

George, G.: JOANNE: Joint dropsonde Observations of the Atmosphere in tropical North atlaNtic meso-scale Environments (v2.0.0), Aeris [data set], https://doi.org/10.25326/246, 2021.

Hersbach, H., Bell, B., Berrisford, P., Hirahara, S., Horányi, A., Muñoz-Sabater, J., Nicolas, J., Peubey, C., Radu, R., Schepers, D., Simmons, A., Soci, C., Abdalla, S., Abellan, X., Balsamo, G., Bechtold, P., Biavati, G., Bidlot, J., Bonavita, M., Chiara, G., Dahlgren, P., Dee, D., Diamantakis, M., Dragani, R., Flemming, J., Forbes, R., Fuentes, M., Geer, A., Haimberger, L., Healy, S., Hogan, R. J., Hólm, E., Janisková, M., Keeley, S., Laloyaux, P., Lopez, P., Lupu, C., Radnoti, G., Rosnay, P., Rozum, I., Vamborg, F., Villaume, S., and Thépaut, J.-N.: The ERA5 global reanalysis, Q. J. Roy. Meteor. Soc., 146, 1999–2049, https://doi.org/10.1002/qj.3803, 2020.

Kölling, T., Zinner, T., and Mayer, B.: Aircraft-based stereographic reconstruction of 3-D cloud geometry, Atmos. Meas. Tech., 12, 1155–1166, https://doi.org/10.5194/amt-12-1155-2019, 2019.

Krautstrunk, M. and Giez, A.: The Transition From FALCON to HALO Era Airborne Atmospheric Research, in:

Atmospheric Physics, Springer Berlin Heidelberg, 609–624, https://doi.org/10.1007/978-3-642-30183-4_37, 2012.

Lucas, B. D. and Kanade, T.: An Iterative Image Registration Technique with an Application to Stereo Vision, in: Proceedings of the 7th International Joint Conference on Artificial Intelligence – Volume 2, IJCAI'81, Morgan Kaufmann Publishers Inc., San Francisco, CA, USA, 674–679, https://hal.science/hal-03697340 (last access: 3 December 2024), 1981.

Mayer, B.: Radiative transfer in the cloudy atmosphere, Eur. Physical J. Conf., 1, 75–99, https://doi.org/10.1140/epjconf/e2009-00912-1, 2009.

Mayer, B. and Kylling, A.: Technical note: The libRadtran software package for radiative transfer calculations – description and examples of use, Atmos. Chem. Phys., 5, 1855–1877, https://doi.org/10.5194/acp-5-1855-2005, 2005.

Mitra, A., Di Girolamo, L., Hong, Y., Zhan, Y., and Mueller, K. J.: Assessment and Error Analysis of Terra-MODIS and MISR Cloud-Top Heights Through Comparison With ISS-CATS Lidar, J. Geophys. Res.-Atmos., 126, e2020JD034281, https://doi.org/10.1029/2020jd034281, 2021.

Moroney, C., Davies, R., and Muller, J.-P.: Operational retrieval of cloud-top heights using MISR data, IEEE T. Geosci. Remote, 40, 1532–1540, https://doi.org/10.1109/tgrs.2002.801150, 2002.

Nakajima, T. and King, M. D.: Determination of the Optical Thickness and Effective Particle Radius of Clouds from Reflected Solar Radiation Measurements. Part I: Theory, J. Atmos. Sci., 47, 1878–1893, https://doi.org/10.1175/1520-0469(1990)047<1878:dotota>2.0.co;2, 1990.

Pörtge, V., Kölling, T., Weber, A., Volkmer, L., Emde, C., Zinner, T., Forster, L., and Mayer, B.: High-spatial-resolution retrieval of cloud droplet size distribution from polarized observations of the cloudbow, Atmos. Meas. Tech., 16, 645–667, https://doi.org/10.5194/amt-16-645-2023, 2023.

Savazzi, A. C. M., Nuijens, L., Sandu, I., George, G., and Bechtold, P.: The representation of the trade winds in ECMWF forecasts and reanalyses during EUREC4A, Atmos. Chem. Phys., 22, 13049–13066, https://doi.org/10.5194/acp-22-13049-2022, 2022.

Seiz, G. and Davies, R.: Reconstruction of cloud geometry from multi-view satellite images, Remote Sens. Environ., 100, 143–149, https://doi.org/10.1016/j.rse.2005.09.016, 2006.

Seiz, G., Davies, R., and Grün, A.: Stereo cloud-top height retrieval with ASTER and MISR, Int. J. Remote Sens., 27, 1839–1853, https://doi.org/10.1080/01431160500380703, 2006.

Stevens, B., Bony, S., Farrell, D., Ament, F., Blyth, A., Fairall, C., Karstensen, J., Quinn, P. K., Speich, S., Acquistapace, C., Aemisegger, F., Albright, A. L., Bellenger, H., Bodenschatz, E., Caesar, K.-A., Chewitt-Lucas, R., de Boer, G., Delanoë, J., Denby, L., Ewald, F., Fildier, B., Forde, M., George, G., Gross, S., Hagen, M., Hausold, A., Heywood, K. J., Hirsch, L., Jacob, M., Jansen, F., Kinne, S., Klocke, D., Kölling, T., Konow, H., Lothon, M., Mohr, W., Naumann, A. K., Nuijens, L., Olivier, L., Pincus, R., Pöhlker, M., Reverdin, G., Roberts, G., Schnitt, S., Schulz, H., Siebesma, A. P., Stephan, C. C., Sullivan, P., Touzé-Peiffer, L., Vial, J., Vogel, R., Zuidema, P., Alexander, N., Alves, L., Arixi, S., Asmath, H., Bagheri, G., Baier, K., Bailey, A., Baranowski, D., Baron, A., Barrau, S., Barrett, P. A., Batier, F., Behrendt, A., Bendinger, A., Beucher, F., Bigorre, S., Blades, E., Blossey, P., Bock, O., Böing, S., Bosser, P., Bourras, D., Bouruet-Aubertot, P., Bower, K., Branellec, P., Branger, H., Brennek, M., Brewer, A., Brilouet, P.-E., Brügmann, B., Buehler, S. A., Burke, E., Burton, R., Calmer, R., Canonici, J.-C., Carton, X., Cato Jr., G., Charles, J. A., Chazette, P., Chen, Y., Chilinski, M. T., Choularton, T., Chuang, P., Clarke, S., Coe, H., Cornet, C., Coutris, P., Couvreux, F., Crewell, S., Cronin, T., Cui, Z., Cuypers, Y., Daley, A., Damerell, G. M., Dauhut, T., Deneke, H., Desbios, J.-P., Dörner, S., Donner, S., Douet, V., Drushka, K., Dütsch, M., Ehrlich, A., Emanuel, K., Emmanouilidis, A., Etienne, J.-C., Etienne-Leblanc, S., Faure, G., Feingold, G., Ferrero, L., Fix, A., Flamant, C., Flatau, P. J., Foltz, G. R., Forster, L., Furtuna, I., Gadian, A., Galewsky, J., Gallagher, M., Gallimore, P., Gaston, C., Gentemann, C., Geyskens, N., Giez, A., Gollop, J., Gouirand, I., Gourbeyre, C., de Graaf, D., de Groot, G. E., Grosz, R., Güttler, J., Gutleben, M., Hall, K., Harris, G., Helfer, K. C., Henze, D., Herbert, C., Holanda, B., Ibanez-Landeta, A., Intrieri, J., Iyer, S., Julien, F., Kalesse, H., Kazil, J., Kellman, A., Kidane, A. T., Kirchner, U., Klingebiel, M., Körner, M., Kremper, L. A., Kretzschmar, J., Krüger, O., Kumala, W., Kurz, A., L'Hégaret, P., Labaste, M., Lachlan-Cope, T., Laing, A., Landschützer, P., Lang, T., Lange, D., Lange, I., Laplace, C., Lavik, G., Laxenaire, R., Le Bihan, C., Leandro, M., Lefevre, N., Lena, M., Lenschow, D., Li, Q., Lloyd, G., Los, S., Losi, N., Lovell, O., Luneau, C., Makuch, P., Malinowski, S., Manta, G., Marinou, E., Marsden, N., Masson, S., Maury, N., Mayer, B., Mayers-Als, M., Mazel, C., McGeary, W., McWilliams, J. C., Mech, M., Mehlmann, M., Meroni, A. N., Mieslinger, T., Minikin, A., Minnett, P., Möller, G., Morfa Avalos, Y., Muller, C., Musat, I., Napoli, A., Neuberger, A., Noisel, C., Noone, D., Nordsiek, F., Nowak, J. L., Oswald, L., Parker, D. J., Peck, C., Person, R., Philippi, M., Plueddemann, A., Pöhlker, C., Pörtge, V., Pöschl, U., Pologne, L., Posyniak, M., Prange, M., Quiñones Meléndez, E., Radtke, J., Ramage, K., Reimann, J., Renault, L., Reus, K., Reyes, A., Ribbe, J., Ringel, M., Ritschel, M., Rocha, C. B., Rochetin, N., Röttenbacher, J., Rollo, C., Royer, H., Sadoulet, P., Saffin, L., Sandiford, S., Sandu, I., Schäfer, M., Schemann, V., Schirmacher, I., Schlenczek, O., Schmidt, J., Schröder, M., Schwarzenboeck, A., Sealy, A., Senff, C. J., Serikov, I., Shohan, S., Siddle, E., Smirnov, A., Späth, F., Spooner, B., Stolla, M. K., Szkółka, W., de Szoeke, S. P., Tarot, S., Tetoni, E., Thompson, E., Thomson, J., Tomassini, L., Totems, J., Ubele, A. A., Villiger, L., von Arx, J., Wagner, T., Walther, A., Webber, B., Wendisch, M., Whitehall, S., Wiltshire, A., Wing, A. A., Wirth, M., Wiskandt, J., Wolf, K., Worbes, L., Wright, E., Wulfmeyer, V., Young, S., Zhang, C., Zhang, D., Ziemen, F., Zinner, T., and Zöger, M.: EUREC^{4}A, Earth Syst. Sci. Data, 13, 4067–4119, https://doi.org/10.5194/essd-13-4067-2021, 2021.

Volkmer, L., Kölling, T., Zinner, T., and Mayer, B.: 3-D cloud geometry from 2-D radiance measurements of specMACS during EUREC4A using a stereographic approach, Aeris [data set], https://doi.org/10.25326/508, 2023.

Volkmer, L., Pörtge, V., Jakub, F., and Mayer, B.: Model-based evaluation of cloud geometry and droplet size retrievals from two-dimensional polarized measurements of specMACS, Atmos. Meas. Tech., 17, 1703–1719, https://doi.org/10.5194/amt-17-1703-2024, 2024.

Weber, A., Kölling, T., Pörtge, V., Baumgartner, A., Rammeloo, C., Zinner, T., and Mayer, B.: Polarization upgrade of specMACS: calibration and characterization of the 2D RGB

polarization-resolving cameras, Atmos. Meas. Tech., 17, 1419–1439, https://doi.org/10.5194/amt-17-1419-2024, 2024.

Wendisch, M., Crewell, S., Ehrlich, A., Herber, A., Kirbus, B., Lüpkes, C., Mech, M., Abel, S. J., Akansu, E. F., Ament, F., Aubry, C., Becker, S., Borrmann, S., Bozem, H., Brückner, M., Clemen, H.-C., Dahlke, S., Dekoutsidis, G., Delanoë, J., De La Torre Castro, E., Dorff, H., Dupuy, R., Eppers, O., Ewald, F., George, G., Gorodetskaya, I. V., Grawe, S., Groß, S., Hartmann, J., Henning, S., Hirsch, L., Jäkel, E., Joppe, P., Jourdan, O., Jurányi, Z., Karalis, M., Kellermann, M., Klingebiel, M., Lonardi, M., Lucke, J., Luebke, A. E., Maahn, M., Maherndl, N., Maturilli, M., Mayer, B., Mayer, J., Mertes, S., Michaelis, J., Michalkov, M., Mioche, G., Moser, M., Müller, H., Neggers, R., Ori, D., Paul, D., Paulus, F. M., Pilz, C., Pithan, F., Pöhlker, M., Pörtge, V., Ringel, M., Risse, N., Roberts, G. C., Rosenburg, S., Röttenbacher, J., Rückert, J., Schäfer, M., Schaefer, J., Schemann, V., Schirmacher, I., Schmidt, J., Schmidt, S., Schneider, J., Schnitt, S., Schwarz, A., Siebert, H., Sodemann, H., Sperzel, T., Spreen, G., Stevens, B., Stratmann, F., Svensson, G., Tatzelt, C., Tuch, T., Vihma, T., Voigt, C., Volkmer, L., Walbröl, A., Weber, A., Wehner, B., Wetzel, B., Wirth, M., and Zinner, T.: Overview: quasi-Lagrangian observations of Arctic air mass transformations – introduction and initial results of the HALO–$(\mathcal{AC})^3$ aircraft campaign, Atmos. Chem. Phys., 24, 8865–8892, https://doi.org/10.5194/acp-24-8865-2024, 2024.

Wirth, M.: Cloud top height derived from airborne measurements with the WALES lidar during the EUREC4A field campaign, Aeris [data set], https://doi.org/10.25326/216, 2021.

Wirth, M., Fix, A., Mahnke, P., Schwarzer, H., Schrandt, F., and Ehret, G.: The airborne multi-wavelength water vapor differential absorption lidar WALES: system design and performance, Appl. Phys. B, 96, 201–213, https://doi.org/10.1007/s00340-009-3365-7, 2009.

Wu, L., Su, H., Zeng, X., Posselt, D. J., Wong, S., Chen, S., and Stoffelen, A.: Uncertainty of Atmospheric Winds in Three Widely Used Global Reanalysis Datasets, J. Appl. Meteorol. Clim., 63, 165–180, https://doi.org/10.1175/jamc-d-22-0198.1, 2024.